Explicit meshfree solution for large deformation dynamic problems in saturated porous media

Pedro Navas · Lorenzo Sanavia · Susana López-Querol · Rena C. Yu

Dedicated to the 75th birthday of Professor Bernhard A. Schrefler

Abstract In this paper a new methodology to simulate saturated soils subjected to dynamic loadings under large deformation regime (locally up to 40% in equivalent plastic strain) is presented. The coupling between solid and fluid phases is solved through the complete formulation of the Biot's equations. The additional novelty lies in the employment of an explicit time integration scheme of the $u - w$ (solid displacement – relative fluid displacement) formulation which enables us to take advantage of such explicit schemes. Shape functions based on the principle of maximum entropy implemented in the framework of Optimal Transportation Meshfree schemes are utilized to solve both elastic and plastic problems.

Keywords Biot's equation · Complete formulation · Meshfree · Explicit approach · Large strains

1 Introduction

Modeling saturated soils under dynamic loads is an interesting issue, particularly when dynamic consolidation or quick settlements of soils under large deformations are concerned. However, the research focused on this aspect is scant, the literature being even more limited when finite deformations are involved. This is mainly due to the fact that, on the one hand, the $u - p_w$ (solid displacement – fluid pressure) formulation is widely used in dynamics to solve the coupled problem due to its simplicity (e.g. [10,32,33]), and on the other hand, since fluid accelerations are neglected in this formulation, this makes it impossible to capture high frequency movements when the coupling between soil and water needs to be dealt with [34].

Along the years, depending on the employed formulation for coupled problems (either simplified or complete), on the assumptions (if the accelerations are considered or not) and on the way that the equations are solved (explicit or implicit), different techniques to solve the coupled problem have been developed. The governing equations of the coupled problem were first introduced by Biot [4], then reviewed by Zienkiewicz and co-workers [33–35,32]. There were two alternatives to achieve the same set of equations: one by Zienkiewicz, Chang and Bettes [34], or Zienkiewicz and Shiomi [35, 32] applied at macroscopic scale, the other by Lewis and Schrefler [16] within the Hybrid Mixture Theory starting from the microscopic scale. Both showed that an accurate enough solution can be achieved for low frequency dynamic problems by neglecting the convective and acceleration terms in the complete formulation, deriving the $u - p_w$ formulation.

Regarding the application of $u - p_w$ formulation under large deformation regime, the first works were carried out by Diebels and Ehlers [13], Borja *et al.* [7,8] and Armero [1] who tested their models by simulating the constitutive behavior of the the solid phases with linear elastic, Cam-Clay and Drucker-Prager theories respectively. Around the same period of time, Ehlers and Eipper [14] applied a new Neo-Hookean constitu-

Pedro Navas and Rena C. Yu
School of Civil Engineering, University of Castilla La-Mancha, Avda. Camilo Jose Cela s/n, 13071, Ciudad Real, Spain, E-mail: pedro.navas@uclm.es, rena@uclm.es

Lorenzo Sanavia
Dipartimento di Ingegneria Civile, Edile e Ambientale, Università degli Studi di Padova, via F. Marzolo 9, 35131 Padova, Italy, E-mail: lorenzo.sanavia@unipd.it

Susana López-Querol
Department of Civil, Environmental and Geomatic Engineering, University College London, Gower Street, London WC1E 6BT, UK, E-mail: s.lopez-querol@ucl.ac.uk

tive model to represent the compaction of the soil up to the solid compaction point. All of these researches were solved using implicit schemes where the linearization of the derivatives of the $u - p_w$ equations was necessary. This linearization was also made by Sanavia *et al.*[27] who considered several neglected terms of the previous works and extended the methodology to unsaturated soils [29].

By contrast, the complete formulation valid for all frequencies movements is known to be essential for solving dynamic problems [15, 25]. Nevertheless, the formulation employing the total displacement of the water, U, as a nodal unknown is unstable when large deformations of the fluid phase occur. As an alternative, the employment of the relative water displacements, w, has been proved to be successful [19, 21]. Traditional manner to solve the complete formulation is the utilization of implicit schemes [7, 8, 1, 14] except the recent work of Ye *et al.* [31]. Thus, the current work represents the first one that solves the complete formulation with relative water displacements, $u - w$, using an explicit scheme. Since there is no necessity in formulating the tangent stiffness matrix in an explicit procedure, the complex process of linearization of the governing equations is avoided. In addition, as no matrix inversion is involved, the computational effort is minimized and code parallelization is facilitated.

Moreover, it bears emphasis that the proposed methodology, as it is thought for the finite strain regime, is carried out within a meshfree scheme due to its numerous advantages when large deformations are involved. In particular, the shape functions developed by Arroyo and Ortiz [2] based on the principle of maximum entropy [24] are employed. The spacial domain has been discretized into nodes and material points following the Optimal Transportation Meshfree (OTM) scheme of Li *et al.* [17]. The Drucker-Prager yield criterion, the good performance of which has been demonstrated for large deformation problems [23], is herein adopted.

In contrast to the work of Bandara and Soga [3] or Ceccato and Simonini [11], who made use of two material sets for solid and water phases in their Material Point Method (MPM) schemes, a single set of materials for the coupling between water and solid phases is employed in this work since the relative water displacement is considered. This leads to significant savings on the computational effort. In addition, this formulation is stronger than some others such as the Smooth Particle Hydrodynamics (SPH) since the pore pressure is also computed in the material points. The SPH formulation presents a tensile instability since only one nodal set is employed to contain displacement and stress fields.

The rest of the paper is organized as follows. The Biot's equations are presented next. The constitutive models employed to model the solid behavior are summarized in Section 3. The explicit methodology implemented is elucidated in Section 4. Applications to various problems are illustrated in Section 5. Relevant conclusions are drawn in Section 6. The definitions of all symbols used in the equations are provided in the nomenclature appendix.

2 Biot's equations: u-w-p_w formulation

The Biot's equations [5] are based on formulating the mechanical behavior of a solid-fluid mixture, the coupling between different phases, and the continuity of flux through a differential domain of saturated porous media. Here the balance equations will be derived from Lewis and Schrefler [16] in the spatial setting (see [16] or [28, 29] for the kinematic equations).

As far as the notations are concerned, bold symbols are employed herein for vectors and matrices, and regular letters for scalar variables, are used. Let $\boldsymbol{u}$ and $\boldsymbol{U}$ represent the displacement vector of the solid skeleton and the absolute displacement of the fluid phase respectively. Because in porous media theory is common to describe the fluid motion with respect to the solid, the relative displacement of the fluid phase with respect to the solid one, $\boldsymbol{w}$, is introduced and expressed as [20]

$$\boldsymbol{w} = nS_w \left(\boldsymbol{U} - \boldsymbol{u} \right), \tag{1}$$

where S_w is the degree of water saturation and n the soil porosity. Note that $(\boldsymbol{U} - \boldsymbol{u})$ is usually termed as $\boldsymbol{u}^{ws}$ in the literature [16]. Let ρ, ρ_w and ρ_s respectively represent the mixture, fluid phase and solid particle densities, the mixture density can be defined as function of the porosity:

$$\rho = nS_w\rho_w + (1-n)\rho_s. \tag{2}$$

In the above equations, the porosity, n, is the ratio between the voids volume, V_v, and the total volume, V_T:

$$n = \frac{V_v}{V_T} = \frac{V_v}{V_v + V_s}, \tag{3}$$

where V_s is the volume of the solid grains.

In the current work, the soil is assumed to be totally saturated, i.e. V_v coincides with the water volume, which results S_w equals to one. Meanwhile, the volumetric compressibility of the mixture, Q [33] is calculated as

$$Q = \left[\frac{1-n}{K_s} + \frac{n}{K_w} \right]^{-1}, \tag{4}$$

where K_s is the bulk modulus of the solid grains, whereas K_w is the compressive modulus of the fluid phase (usually water). In addition, by assuming tensile stresses (except pore pressure p_w, which is positive for compression) and strains as positive, the Terzaghi's effective stress [30] is defined as follows

$$\boldsymbol{\sigma} = \boldsymbol{\sigma}' - p_w \mathbf{I}, \tag{5}$$

where $\boldsymbol{\sigma}'$ and $\boldsymbol{\sigma}$ are the respective effective and total Cauchy stress tensors (positive in tension), whereas $\mathbf{I}$ is the second order unit tensor.

Next, we first explain in detail the derivation of mass balance and linear momentum equations for a fluid saturated multiphase media. Then the final $u - w$ formulation is presented.

2.1 Derivation of the mass balance equation

The general mass balance equation in a multiphase media for compressible grains given by Lewis and Schrefler [16] is presented next. Let p_w, p_g represent the water and gas pressures respectively, T, the temperature, then this general mass balance equation is written as follows,

$$\left(\frac{\alpha - n}{K_s} S_w^2 + \frac{n S_w}{K_w} \right) \frac{D^s p_w}{Dt} + \frac{\alpha - n}{K_s} S_w S_g \frac{D^s p_g}{Dt} -$$
$$\beta_{sw} \frac{D^s T}{Dt} + \left(\frac{\alpha - n}{K_s} S_w p_w - \frac{\alpha - n}{K_s} S_w p_g + n \right) \frac{D^s S_w}{Dt} +$$
$$\alpha S_w \mathrm{div}\ \boldsymbol{v}^s + \frac{1}{\rho_w} \mathrm{div}\ (n S_w \rho_w \boldsymbol{v}^{ws}) = -n S_w e^w \tag{6}$$

where the right hand side term represents the quantity of water lost through evaporation for unit time and volume. The thermal expansion coefficient of the solid-fluid mixture, β_{sw}, is a combination of that of the solid, β_s, and the fluid, β_w:

$$\beta_{sw} = S_w [(\alpha - n)\beta_s + n\beta_w]. \tag{7}$$

In addition, α is the Biot's coefficient:

$$\alpha = 1 - \frac{K_T}{K_s}. \tag{8}$$

where K_T denotes the bulk modulus of the solid skeleton. α is usually assumed equal to one in soils as the grains are much more rigid than the mixture. D^s/Dt denotes the material time derivative with respect to the solid.

The relative velocity of the fluid, $\boldsymbol{v}^{ws}$, in Eq. (6) is defined through the generalized Darcy law as [16]

$$n S_w \boldsymbol{v}^{ws} = \frac{k^{rw} \boldsymbol{k}}{\mu_w} [-\mathrm{grad}\ p_w + \rho_w (\boldsymbol{g} - \boldsymbol{a}^s - \boldsymbol{a}^{ws})], \tag{9}$$

where $\boldsymbol{g}$ represents the gravity acceleration vector, $\boldsymbol{a}^s$ and $\boldsymbol{a}^{ws}$ are the solid acceleration and the relative water acceleration with respect to the solid respectively, $\boldsymbol{k}$, the intrinsic permeability tensor of the porous matrix in water saturated condition, k^{rw} is the water relative permeability parameter (a dimensionless parameter varying from zero to one) and μ_w is the dynamic viscosity of the water [Pa · s]. For the case of isotropic permeability, the *intrinsic* permeability, expressed in [m²], is related with the notion of hydraulic conductivity, κ [m/s], by the following equation

$$\frac{k}{\mu_w} = \frac{\kappa}{\rho_w g}. \tag{10}$$

As we consider a totally saturated, iso-thermal multiphase media, $D^s T/Dt = 0, S_g = 0, S_w = 1, k^{rw} = 1$, $e^w = 0$, consequently, $D^s S_w/Dt = 0$. If additionally the fluid density variation is neglected, Eq. (6) is simplified as,

$$\left(\frac{1-n}{K_s} + \frac{n}{K_w} \right) \frac{D^s p_w}{Dt} + \mathrm{div}\ \boldsymbol{v}^s + \mathrm{div}\ (n\boldsymbol{v}^{ws}) = 0. \tag{11}$$

Taking into consideration Eq. (4), the mass balance equation is written as follows:

$$\frac{1}{Q} \frac{D^s p_w}{Dt} + \mathrm{div}\ \dot{\boldsymbol{u}} + \mathrm{div}\ \dot{\boldsymbol{w}} = 0, \tag{12}$$

where the relationships $\dot{\boldsymbol{u}} \equiv \boldsymbol{v}^s$ and $\dot{\boldsymbol{w}} \approx n\boldsymbol{v}^{ws}$ have been introduced. The latter equation has been derived from Eq. (1) computing the material time derivative of $\boldsymbol{w}$ with respect to the solid and neglecting the material time derivative of the porosity with respect to the solid for simplicity. This assumption can be justified by the small time step value usually adopted in dynamics at high frequencies.

When accelerations of the solid and the fluid are negligible, as in the quasi-static $u - p_w$ formulation [28, 29], and the solid grain and the fluid can be considered incompressible, substituting Darcy's law into Eq. (12) we have the mass equation expressed as

$$\mathrm{div}\ \boldsymbol{v}^s + \mathrm{div}\ \left[\frac{\boldsymbol{k}}{\mu_w} (-\mathrm{grad}\ p_w + \rho_w \boldsymbol{g}) \right] = 0. \tag{13}$$

2.2 Linear momentum balance equations

On the one hand, the linear momentum balance equation for the fluid phase was presented in Eq. (9). By rearranging different terms, the following expression is obtained:

$$-\mathrm{grad}\ p_w - \frac{\mu_w}{k} \dot{\boldsymbol{w}} + \rho_w \left(\boldsymbol{g} - \ddot{\boldsymbol{u}} - \frac{\ddot{\boldsymbol{w}}}{n} \right) = \mathbf{0}, \tag{14}$$

where the relationships $\ddot{\boldsymbol{u}} \equiv \boldsymbol{a}^s$ and $\ddot{\boldsymbol{w}} \approx n\boldsymbol{a}^{ws}$ have been introduced (neglecting, similarly to the derivation of Eq. (12), the material time derivative of the porosity with respect to the solid). On the other hand, according to Lewis and Schrefler [16], the linear momentum balance equation for the multiphase system can also be expressed as the summation of the dynamic equations for the individual constituents relative to the solid as, i.e.,

$$-\rho\boldsymbol{a}^s - nS_w\rho_w\boldsymbol{a}^{ws} - nS_g\rho_g\boldsymbol{a}^{gs} + \text{div }\boldsymbol{\sigma} + \rho\boldsymbol{g} = \boldsymbol{0}, \quad (15)$$

where the convective terms related to $\boldsymbol{a}^{ws}$ and $\boldsymbol{a}^{gs}$ have been neglected. Since in the present research there is no gassy phase as the soil will be considered as totally saturated, $S_g = 0$; $nS_w\rho_w\boldsymbol{a}^{ws} = \rho_w\ddot{\boldsymbol{w}}$, plug Eq. (5) into Eq. (15), the linear momentum equation can be written as follows

$$\text{div }[\boldsymbol{\sigma}' - p_w\,\mathbf{I}] - \rho\ddot{\boldsymbol{u}} - \rho_w\ddot{\boldsymbol{w}} + \rho\boldsymbol{g} = \boldsymbol{0}. \quad (16)$$

2.3 The $u - w$ formulation

The $u - w$ formulation starts from the assumption that Eq. (12) can be integrated over time, i.e.,

$$p_w = -Q\left(\text{div }\boldsymbol{u} + \text{div }\boldsymbol{w}\right) + p_{w0}. \quad (17)$$

Consequently, substituting Eq. (17) into Eq. (14) and Eq. (16) the governing equations for the $u - w$ formulation are obtained as follows

$$\text{div }[\boldsymbol{\sigma}' + Q\left(\text{div }\boldsymbol{u} + \text{div }\boldsymbol{w}\right)\mathbf{I}]$$
$$-\rho\ddot{\boldsymbol{u}} - \rho_w\ddot{\boldsymbol{w}} + \rho\boldsymbol{g} = \boldsymbol{0}, \quad (18)$$

$$Q\,\text{grad}\left[\text{div }\boldsymbol{u} + \text{div}\boldsymbol{w}\right] - \frac{\mu_w}{k}\dot{\boldsymbol{w}}$$
$$+\rho_w\left(\boldsymbol{g} - \ddot{\boldsymbol{u}} - \frac{\ddot{\boldsymbol{w}}}{n}\right) = \boldsymbol{0}. \quad (19)$$

3 Constitutive models for the solid phase

In this Section, we describe the two types of material models implemented to assess the performance of the formulation presented in Section 2. One is for elastic behavior, the other one involves plastic deformation which follows the Drucker-Prager failure criterion.

3.1 Neo-Hookean material model extended to compressible range

One of the widely used material model for predicting non-linear elastic behavior for solids undergoing large deformations is the Neo-Hookean model extended to compressible range. Under spacial configurations, it is expressed as follows [6]:

$$\boldsymbol{\tau}' = J\boldsymbol{\sigma}' = G(\boldsymbol{b} - \mathbf{I}) + (\lambda \ln J)\mathbf{I}, \quad (20)$$

where $\boldsymbol{\tau}'$ and $\boldsymbol{b}$ are the effective Kirchhoff stress tensor and the left Cauchy-Green tensor respectively, whereas J is the Jacobian determinant, G and λ are the Lamé constants.

In order to take into consideration the compaction point of the soil, Ehlers and Eipper [14] presented a modification of the Neo-Hookean law taking into account the influence of the initial porosity n_0 and the Jacobian, i.e.

$$\boldsymbol{\tau}' = G(\boldsymbol{b} - \mathbf{I}) + \lambda\,n_0^2\left(\frac{J}{n_0} - \frac{J}{J - 1 + n_0}\right)\mathbf{I}, \quad (21)$$

which is going to be used for the validation examples in Section 5.

3.2 Drucker-Prager yield criterion

For the calculation of plastic deformations, we follow the work of Cuitiño and Ortiz [12] to relate the right Cauchy-Green strain tensor $\mathbf{C}$ and the small strain tensor $\boldsymbol{\varepsilon}$, during the trial step. In other words, for the current loading step, $k + 1$, the trial elastic deformations, pressure (p_{k+1}^{trial}) and the deviatoric stress tensor ($\mathbf{s}_{k+1}^{trial}$) are computed as the elastic deformations, pressure and the deviatoric stress tensor are computed as:

$$\mathbf{C}_{k+1}^{e\ trial} = (\mathbf{F}_k^p)^{-T}\mathbf{C}_{k+1}(\mathbf{F}_k^p)^{-1}, \quad (22)$$

$$\boldsymbol{\varepsilon}_{k+1}^{e\ trial} = \frac{1}{2}\log\mathbf{C}_{k+1}^{e\ trial}, \quad (23)$$

$$p_{k+1}^{trial} = K\,(\varepsilon_{vol}^e)_{k+1}^{trial}, \quad (24)$$

$$\mathbf{s}_{k+1}^{trial} = 2G\,(\varepsilon_{dev}^e)_{k+1}^{trial}. \quad (25)$$

where K and G represent the bulk and shear moduli of the solid respectively. Once the incremental plastic strain tensor is known, the plastic deformation gradient can be derived as:

$$\Delta\mathbf{F}_{k+1}^p = \exp(\Delta\boldsymbol{\varepsilon}_{k+1}^p), \quad (26)$$

$$\mathbf{F}_{k+1}^p = \Delta\mathbf{F}_{k+1}^p\mathbf{F}_k^p. \quad (27)$$

Regarding the Drucker-Prager yield criterion, the methodology of Sanavia et al. [29, 26] is employed for its reduced computational effort and its capacity to distinguish if the location of the stress state is on the cone or apex before calculating the plastic strain. The current cohesion, c_{k+1}, and its derivative, the hardening modulus, H, are calculated following Camacho and Ortiz research [9] from the reference value, c_0, the reference

Table 1 Equivalent plastic strain

Classical	$\bar{\varepsilon}^p_{k+1} = \bar{\varepsilon}^p_k + \Delta\gamma\sqrt{3\alpha_Q^2 + 1}$
Apex	$\bar{\varepsilon}^p_{k+1} = \bar{\varepsilon}^p_k + \sqrt{\Delta\gamma_1^2 + 3\alpha_Q^2\left(\Delta\gamma_1 + \Delta\gamma_2\right)^2}$

Table 2 Parameters for Drucker-Prager and von-Mises yield criteria

	DP: Plane strain	DP: Outer cone	von-Mises
α_F	$\frac{\tan\phi}{\sqrt{3+4\tan^2\phi}}\sqrt{\frac{2}{3}}$	$\frac{2\sin\phi}{3-\sin\phi}\sqrt{\frac{2}{3}}$	0
α_Q	$\frac{\tan\psi}{\sqrt{3+4\tan^2\psi}}\sqrt{\frac{2}{3}}$	$\frac{2\sin\psi}{3-\sin\psi}\sqrt{\frac{2}{3}}$	0
β	$\frac{3}{\sqrt{3+4\tan^2\phi}}\sqrt{\frac{2}{3}}$	$\frac{6\cos\phi}{3-\sin\phi}\sqrt{\frac{2}{3}}$	$\sqrt{\frac{2}{3}}$

plastic strain, ε_0, and the hardening exponent, N^ε, as follows:

$$c_{k+1} = c_0\left(1 + \frac{\bar{\varepsilon}^p_{k+1}}{\varepsilon_0}\right)^{\frac{1}{N^\varepsilon}},$$

$$\frac{\partial c}{\partial\bar{\varepsilon}^p} = H = \frac{c_0}{N^\varepsilon\varepsilon_0}\left(1 + \frac{\bar{\varepsilon}^p_{k+1}}{\varepsilon_0}\right)^{\left(\frac{1}{N^\varepsilon}-1\right)}, \qquad (28)$$

where $\bar{\varepsilon}^p_{k+1}$ is the current equivalent plastic strain, calculated in different ways depending on the fact that if the stress state is in the classical or apex region, see Table 1.

In order to know which algorithm to employ, a limit value for the pressure, p_{lim} is calculated:

$$p_{lim} = \frac{3\alpha_Q K}{2G}\|\mathbf{s}^{trial}_{k+1}\|$$
$$+ \frac{\beta}{3\alpha_F}\left(\frac{\|\mathbf{s}^{trial}_{k+1}\|}{2G}H\sqrt{1 + 3\alpha_Q^2} + c_k\right). \qquad (29)$$

If the trial pressure is lower than this limit, classical return-mapping algorithm is employed, otherwise the apex algorithm is adopted.

The yield conditions for the classical and apex regions respectively are:

$$\Phi^{cl} = \|\mathbf{s}^{trial}_{k+1}\| - 2G\Delta\gamma + 3\alpha_F[p^{trial}_{k+1} - 3K\alpha_Q\Delta\gamma]$$
$$- \beta c_{k+1}, \qquad (30)$$
$$\Phi^{ap} = \frac{\beta}{3\alpha_F}\left[c_k + H\sqrt{\Delta\gamma_1^2 + 3\alpha_Q^2(\Delta\gamma_1 + \Delta\gamma_2)^2}\right]$$
$$- p^{trial}_{k+1} + 3K\alpha_Q\left(\Delta\gamma_1 + \Delta\gamma_2\right), \qquad (31)$$

where $\Delta\gamma_1 = \frac{\|\mathbf{s}^{trial}_{k+1}\|}{2G}$, $\Delta\gamma$ and $\Delta\gamma_2$ are the objective functions to be calculated in the Newton-Raphson scheme for the classical or apex regions accordingly.

For the calculation of the Drucker-Prager parameters from the friction angle, ϕ, and the dilatancy angle, ψ, the plane strain case is presented in Table 2. Additionally the parameters for the out cone are shown in Table 2. This cone circumscribes the Mohr-Coulomb plastic region, and the corresponding values for a von Mises criterion.

4 Solution dependent the time: Explicit solution

To solve the aforementioned coupled problem in the time domain, the standard central difference explicit Newmark time integration scheme is employed. Consequently, the numerical stability is guaranteed when the Courant-Friedrichs-Lewy (CFL) condition is satisfied. In particular, the time step, Δt, should be small enough to ensure that the compressive wave can travel between nodes, i.e.

$$\Delta t < \frac{h}{V_c}, \qquad (32)$$

where h represents the discretization size and V_c is the p-wave velocity (see [34]), which is defined by

$$V_c = \sqrt{\left(D + \frac{K_f}{n}\right)\frac{1}{\rho}}, \quad \text{where} \quad D = \frac{2G(1-\nu)}{1-2\nu}. \qquad (33)$$

If the current time step is numbered as $k+1$, and assuming the solution in the previous step k has been already obtained (hence it is known), a relationship between $\mathbf{u}_{k+1}$, $\dot{\mathbf{u}}_{k+1}$ and $\ddot{\mathbf{u}}_{k+1}$ is established according to a finite difference scheme, as follows:

$$\ddot{\mathbf{u}}_{k+1} = \ddot{\mathbf{u}}_k + \Delta\ddot{\mathbf{u}}_{k+1},$$
$$\dot{\mathbf{u}}_{k+1} = \dot{\mathbf{u}}_k + \ddot{\mathbf{u}}_k\Delta t + \gamma\Delta t\Delta\ddot{\mathbf{u}}_{k+1},$$
$$\mathbf{u}_{k+1} = \mathbf{u}_k + \dot{\mathbf{u}}_k\Delta t + \frac{1}{2}\Delta t^2\ddot{\mathbf{u}}_k + \beta\Delta t^2\Delta\ddot{\mathbf{u}}_{k+1}. \qquad (34)$$

When the Newmark scheme parameters, γ and β are set to 0.5 and 0 respectively, the central difference scheme is obtained.

4.1 Explicit integration

From Eq. (14) and Eq. (16) we can get the solutions of the acceleration of the solid phase in both cases, written in the incremental form:

$$\Delta\ddot{\mathbf{u}} = \rho^{-1}\left[\boldsymbol{\nabla}\left(\Delta\boldsymbol{\sigma}' - \Delta p_w\right) - \rho_w\Delta\ddot{\mathbf{w}} + \rho\Delta\mathbf{g}\right], \qquad (35)$$
$$\Delta\ddot{\mathbf{u}} = \rho_w^{-1}\left[-\boldsymbol{\nabla}\Delta p_w - \frac{1}{k}\Delta\dot{\mathbf{w}} - \frac{\rho_w}{n}\Delta\ddot{\mathbf{w}} + \rho_w\Delta\mathbf{g}\right]. \qquad (36)$$

As $\Delta\dot{\mathbf{w}}$ is unknown in the $k+1$ step, it is necessary to write the Newmark's time integration scheme from

Eq. (34) in terms of the fluid phase:

$$\Delta \dot{\boldsymbol{w}}_{k+1} = \ddot{\boldsymbol{w}}_k \Delta t + \gamma \Delta t \Delta \ddot{\boldsymbol{w}}_{k+1}, \tag{37}$$

$$\Delta \boldsymbol{w}_{k+1} = \dot{\boldsymbol{w}}_k \Delta t + \frac{1}{2} \Delta t^2 \ddot{\boldsymbol{w}}_k + \beta \Delta t^2 \Delta \ddot{\boldsymbol{w}}_{n+1}. \tag{38}$$

If we write Eq. (36) by substituting $\Delta \dot{\boldsymbol{w}}$ by the definition given in Eq. (37), we obtain:

$$\begin{aligned}
\Delta \ddot{\boldsymbol{u}}_{k+1} &= \rho_w^{-1} \left(-\boldsymbol{\nabla} \Delta p_{w_{k+1}} - \frac{1}{k} \ddot{\boldsymbol{w}}_k \Delta t - \frac{1}{k} \gamma \Delta t \Delta \ddot{\boldsymbol{w}}_{k+1} \right. \\
&\qquad \left. - \frac{\rho_w}{n} \Delta \ddot{\boldsymbol{w}}_{k+1} + \rho_w \, \Delta \boldsymbol{g}_{k+1} \right) \\
&= \rho_w^{-1} \left[-\boldsymbol{\nabla} \Delta p_{w_{k+1}} - \frac{1}{k} \ddot{\boldsymbol{w}}_k \Delta t + \rho_w \, \Delta \boldsymbol{g}_{k+1} \right. \\
&\qquad \left. - \left(\frac{1}{k} \gamma \Delta t + \frac{\rho_w}{n} \right) \Delta \ddot{\boldsymbol{w}}_{k+1} \right]. \tag{39}
\end{aligned}$$

Rearranging Eq. (35) and Eq. (39) we can obtain one equation in terms of the relative acceleration of the fluid, which can be solved explicitly and $\Delta \ddot{\boldsymbol{w}}$ is obtained as in Eq.(41). Once this equation is solved, $\Delta \ddot{\boldsymbol{u}}$ can be obtained from Eq. (35).

$$\begin{aligned}
\rho_w &\left[\boldsymbol{\nabla} \left(\Delta \boldsymbol{\sigma'} - \Delta p_w \right)_{k+1} - \rho_w \, \Delta \ddot{\boldsymbol{w}}_{k+1} + \rho \, \Delta \boldsymbol{g}_{k+1} \right] \\
&= \rho \left[-\boldsymbol{\nabla} \Delta p_{w_{k+1}} - \frac{1}{k} \ddot{\boldsymbol{w}}_k \Delta t \right. \\
&\qquad \left. - \left(\frac{1}{k} \gamma \Delta t + \frac{\rho_w}{n} \right) \Delta \ddot{\boldsymbol{w}}_{k+1} + \rho_w \, \Delta \boldsymbol{g}_{k+1} \right]. \tag{40}
\end{aligned}$$

$$\begin{aligned}
\rho_w \Delta \boldsymbol{R}^s_{k+1} &- (\rho_w - \rho) \Delta \boldsymbol{R}^w_{k+1} + \rho_w \Delta \boldsymbol{P}^s_{k+1} - \rho \Delta \boldsymbol{P}^w_{k+1} \\
&+ \Delta t \rho \frac{1}{k} \ddot{\boldsymbol{w}}_k = \left(\rho_w \rho - \rho \frac{1}{k} \gamma \Delta t - \frac{\rho \rho_w}{n} \right) \Delta \ddot{\boldsymbol{w}}_{k+1}. \tag{41}
\end{aligned}$$

Both equations to be solved, Eq. (41) and Eq. (35), after integration in space can be written in the matrix form in the following way:

$$\begin{aligned}
\left[\boldsymbol{M}^w \boldsymbol{M}^w - \gamma \Delta t \boldsymbol{M}^s \boldsymbol{C} - \frac{\boldsymbol{M}^s \boldsymbol{M}^w}{n} \right]^{-1} & \\
\left[\Delta \boldsymbol{R}^*_{k+1} + \Delta \boldsymbol{P}^*_{k+1} + \Delta t \boldsymbol{M}^s \boldsymbol{C} \ddot{\boldsymbol{w}}_k \right] & \\
= \Delta \ddot{\boldsymbol{w}}_{k+1}, & \tag{42}
\end{aligned}$$

$$\left[\boldsymbol{M}^s \right]^{-1} \left[\Delta \boldsymbol{R}^s + \Delta \boldsymbol{R}^w + \Delta \boldsymbol{P}^s - \boldsymbol{M}^w \Delta \ddot{\boldsymbol{w}} \right]_{k+1} = \Delta \ddot{\boldsymbol{u}}_{k+1}. \tag{43}$$

In Eqs. (42-43), $\boldsymbol{R}_{k+1}$ represents the internal forces of the previous step for the solid, s, fluid, w, or the mixture of both, $*$, i.e.:

$$\begin{aligned}
\Delta \boldsymbol{R}^s_{k+1} &= \boldsymbol{\nabla} \Delta \boldsymbol{\sigma'}_{k+1}, \\
\Delta \boldsymbol{R}^w_{k+1} &= \boldsymbol{\nabla} \Delta p_{w_{k+1}}, \\
\Delta \boldsymbol{R}^*_{k+1} &= \rho_w \Delta \boldsymbol{R}^s_{k+1} - (\rho_w - \rho) \Delta \boldsymbol{R}^w_{k+1}.
\end{aligned}$$

Similarly, the current external forces can be expressed as $\boldsymbol{P}_{k+1}$, containing both gravity acceleration and the boundary conditions for nodal forces. The external forces of the mixture are denoted by:

$$\Delta \boldsymbol{P}^*_{k+1} = \rho_w \Delta \boldsymbol{P}^s_{k+1} - \rho \Delta \boldsymbol{P}^w_{k+1}.$$

Mass and damping matrices, in the $k + 1$ step, are defined as follows:

$$\begin{aligned}
\boldsymbol{M}^w &= \rho_w \boldsymbol{I}, \\
\boldsymbol{M}^s &= \rho \boldsymbol{I}, \\
\boldsymbol{C} &= \frac{1}{k} \boldsymbol{I}.
\end{aligned}$$

4.2 Explicit algorithm within the OTM framework

The pseudo-algorithm of the whole model can be written in the following way:

1. Explicit Newmark Predictor ($\gamma = 0.5$, $\beta = 0$)

$$\begin{aligned}
u_{k+1} &= u_k + \Delta t \dot{u}_k + 0.5 \Delta t^2 \, \ddot{u}_k = u_k + \Delta u_{k+1}, \\
w_{k+1} &= w_k + \Delta t \dot{w}_k + 0.5 \Delta t^2 \, \ddot{w}_k = w_k + \Delta w_{k+1}; \\
\dot{u}_{k+1} &= \dot{u}_k + (1 - \gamma) \Delta t \, \ddot{u}_k, \\
\dot{w}_{k+1} &= \dot{w}_k + (1 - \gamma) \Delta t \, \ddot{w}_k; \\
x_{k+1} &= x_k + \Delta u_{k+1}.
\end{aligned}$$

2. Material points position update

$$x^p_{k+1} = x^p_k + \sum_{a=1}^{Nb} \Delta u^a_{k+1} N^a(x^p_k).$$

3. Deformation gradient calculation

$$\begin{aligned}
\Delta \mathbf{F}_{k+1} &= I + \sum_{a=1}^{Nb} \Delta u^a_{k+1} \nabla N^a(x^p_k), \\
\Delta \mathbf{F}^w_{k+1} &= I + \sum_{a=1}^{Nb} \Delta w^a_{k+1} \nabla N^a(x^p_k), \\
\mathbf{F}_{k+1} &= \Delta \mathbf{F}_{k+1} \mathbf{F}_k, \\
V &= J V_0 = \det \mathbf{F} \, V_0, \\
n &= 1 - \frac{1 - n_0}{J}.
\end{aligned}$$

4. Small strains and pore pressure: $\mathbf{C} = \mathbf{F}^T \mathbf{F}$.

$$\begin{aligned}
\mathrm{div} \, (\boldsymbol{u}) &= \mathrm{tr}(\boldsymbol{\varepsilon}_{k+1}) = \mathrm{tr} \left(\frac{1}{2} \log \mathbf{C}_{k+1} \right), \\
\mathrm{div} \, (\boldsymbol{w}) &= \mathrm{tr}(\boldsymbol{\varepsilon}^w_{k+1}) = \mathrm{tr} \left(\frac{1}{2} \log \mathbf{C}^w_{k+1} \right), \\
p_w &= -Q \, (\mathrm{div} \, \boldsymbol{u} + \mathrm{div} \, \boldsymbol{w}).
\end{aligned}$$

5. Remapping loop, reconnect the nodes with their new material neighbors.

6. Update density and recompute lumped mass

$$\rho_{k+1} = n_{k+1}\rho_w + (1 - n_{k+1})\rho_s.$$

7. Constitutive relations from the Elasto-Plastic model: $\boldsymbol{\sigma'}_{k+1}$ and $\boldsymbol{R}_{k+1}$.

8. Solve Eqs. 42 and 43 for $\ddot{\boldsymbol{u}}_{k+1}$ and $\ddot{\boldsymbol{w}}_{k+1}$.

9. Explicit Newmark Corrector

$$\dot{u}_{k+1} = \dot{u}_{k+1} + \gamma \Delta t \, \ddot{u}_{k+1},$$

$$\dot{w}_{k+1} = \dot{w}_{k+1} + \gamma \Delta t \, \ddot{w}_{k+1}.$$

In order to obtain the material point position (Step 2.) and the deformation gradient (Step 3.) it is necessary to calculate the shape function and its derivatives. Since a meshfree method is employed, the computation is done along a neighborhood N_b. As mentioned before, the shape functions are based on the work of Arroyo and Ortiz [2], who defined the Local Max-Ent shape function (LME) of the point (x) with respect to the neighborhood (x_a) as follows:

$$N_a(\mathbf{x}) = \frac{\exp\left[-\beta \left|\mathbf{x} - \mathbf{x_a}\right|^2 + \boldsymbol{\lambda}^* \cdot (\mathbf{x} - \mathbf{x_a})\right]}{Z(\mathbf{x}, \boldsymbol{\lambda}^*(\mathbf{x}))}, \qquad (44)$$

where

$$Z(\mathbf{x}, \boldsymbol{\lambda}) = \sum_{a=1}^{Nb} \exp\left[-\beta \left|\mathbf{x} - \mathbf{x_a}\right|^2 + \boldsymbol{\lambda} \cdot (\mathbf{x} - \mathbf{x_a})\right]. \quad (45)$$

The first derivatives of the shape function can be obtained from the own shape function and its Hessian matrix $\mathbf{J}$ by employing the following expression:

$$\nabla N_a^* = -N_a^* (\mathbf{J}^*)^{-1} (\mathbf{x} - \mathbf{x_a}), \qquad (46)$$

The parameter β defines the shape of the neighborhood and it is related with the discretization size (or nodal spacing), h, and the constant, γ, which controls the locality of the shape functions, as follows,

$$\beta = \frac{\gamma}{h^2}. \qquad (47)$$

It bears emphasis that $\boldsymbol{\lambda}^*(\mathbf{x})$ comes from the minimization of the function $g(\boldsymbol{\lambda}) = \log Z(\mathbf{x}, \boldsymbol{\lambda})$ to guarantee the maximum entropy, by employing a modified Nelder-Mead algorithm [23].

It is important to clarify the remapping loop defined in the algorithm. By using the stretches, λ_1, λ_2 and λ_3, the eigenvalues of the Right Cauchy-Green deformation tensor, the neighborhood of the shape function can be enlarged. This fact allows us to model large deformation problems since the new locations of material points and nodes lead to new values of the shape function. When the largest stretch surpasses a tolerance it is necessary to do the following:
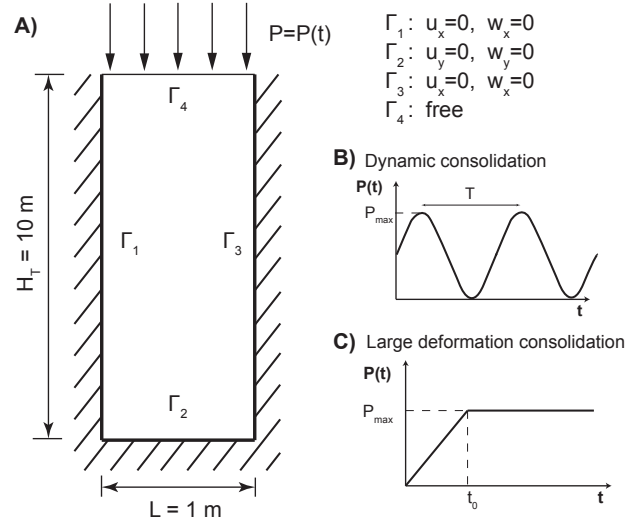

Fig. 1 A) Geometry and boundary conditions of the column of soil; Loading of B) the dynamic consolidation and C) large deformation consolidation problems.

– Update neighborhood and parameter $\beta_{k+1}^p < \beta_k^p$, see Eq. (44) and Eq. (45).
– Recompute $N^a(x_{k+1}^p)$ and $\nabla N^a(x_{k+1}^p)$ with the new positions of x_{k+1} and x_{k+1}^p.

5 Validation

In order to validate the proposed methodology, three examples are presented in this Section. The first one is the elastic dynamic consolidation proposed by Zienkiewicz *et al.* [34] to assess the performance of the complete formulation when large accelerations are involved. The second one is a consolidation problem for large deformations up to 1.5 meters. Finally the formation of a plastic shear band in a square domain is demonstrated by employing the Drucker-Prager yield criterion.

5.1 Dynamic consolidation

The dynamic consolidation of a soil column is studied using the geometry given in Fig. 1.A. The column is loaded at the top boundary, Γ_4, by a harmonic surface loading, $\cos(\omega t)$, see Fig. 1.B, where the angular frequency ω is defined as $2\pi/T$. This problem was first analytically solved by Zienkiewicz *et al.* [34] in 1980s, and more recently by Navas *et al.* [22] using an implicit meshfree Eulerian framework using shape functions based on the principle of local maximum entropy.

Different soil behaviors studied in the aforementioned work are dependent on the the solid skeleton properties,
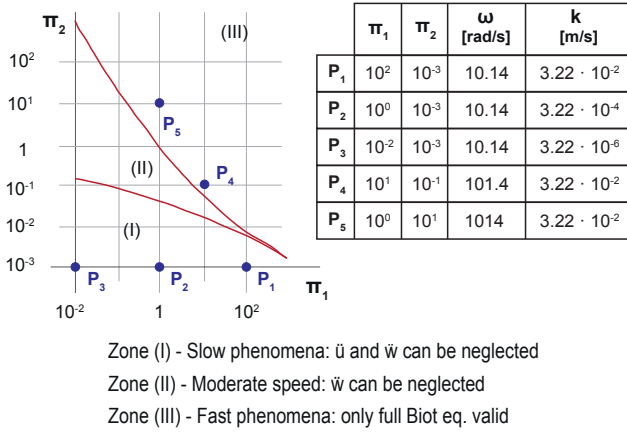
Zone (I) - Slow phenomena: ü and ẅ can be neglected

Zone (II) - Moderate speed: ẅ can be neglected

Zone (III) - Fast phenomena: only full Biot eq. valid

Fig. 2 Zones of the different behavior of the soil depending on the parameters Π_1 and Π_2 and values of ω and k for the different points to be studied.

the permeability and the angular frequency of the harmonic load. Three zones, defined in Fig. 2 can be distinguished according to the values of Π_1 and Π_2, which are defined as follows:

$$\Pi_1 = \frac{k\,V_c^2}{g\,\frac{\rho_f}{\rho}\,\omega\,H_T^2} = \frac{k\,\omega}{g\,\frac{\rho_f}{\rho}\,\Pi_2}, \quad \Pi_2 = \frac{\omega^2\,H_T^2}{V_c^2} \qquad (48)$$

where H_T is the column height, V_c is the p-wave velocity (see Eq. 4). While Π_2 is closely related with ratio between the frequency of the loading and the natural frequency of the system, Π_1 combines this ratio together with the influence of the hydraulic conductivity. Specifically, Zone I is characterized as slow phenomenon where both solid and fluid accelerations can be neglected; Zone II is typical of moderate speed behavior, where only the fluid phase inertia is negligible; in Zone III, however, inertial contributions from both solid and fluid phases are significant and cannot be neglected. The five different points studied herein are shown in Fig 2, where the loading frequency, ω, and the soil permeability, k, are also listed.

The material parameters are provided in Tab 3, and they are chosen to fit the dimensionless parameters employed by Zienkiewicz et al.[34]. For this problem and the following one, the space discretization is of 0.2 m (316 nodes, 500 material points) and the time step employed is 50 μs.

The maximum envelope of the dimensionless pore pressure along the column is depicted in Figs. 3 and 4. Both figures show a very good agreement between the solution given by Navas et al. [22] and the one obtained with the current methodology. The main difference lies in the fact that the current solutions present more oscillations compared to the original ones. This trend can be more clearly seen in Fig. 4 for the two points, P4 and

Table 3 Material parameters for the dynamic consolidation problem

G [MPa]	312.5	K_w [MPa]	10^4
ν	0.2	K_s [MPa]	10^{34}
n	0.333	ρ_w [kg/m^3]	1000
V_c [m/s]	3205	ρ_s [kg/m^3]	3003
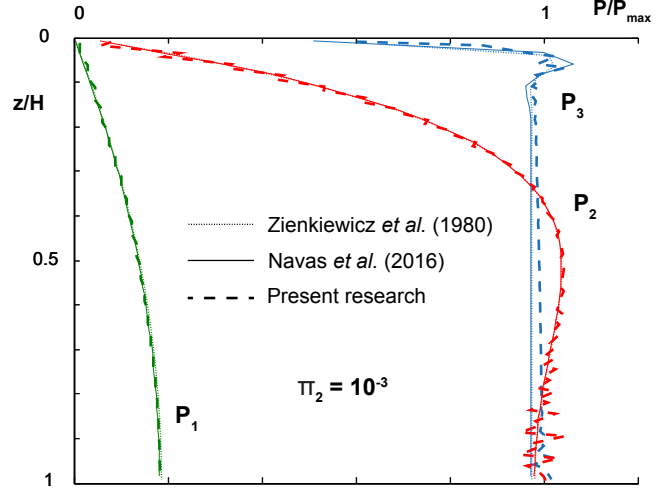
Fig. 3 Maximum envelopes of the isochrones of the pore pressure for points P_1 to P_3 ($\Pi_2 = 10^{-3}$).
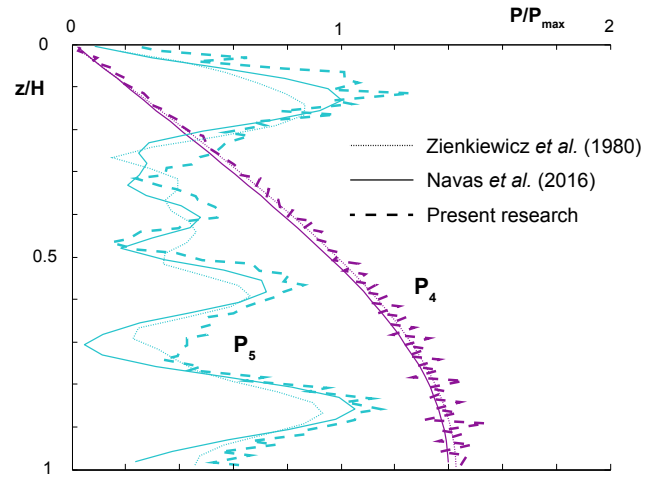
Fig. 4 Maximum envelopes of the isochrones of the pore pressure for points P_4 and P_5.

Table 4 Material parameters of the dynamic consolidation problem

λ [MPa]	29	K_w [MPa]	2.2×10^4
G [MPa]	7	K_s [MPa]	10^{34}
n	0.42	ρ_w [kg/m³]	1000
k [m/s]	0.1	ρ_s [kg/m³]	2700

P5, both located in zone III. This is due to the different time integration scheme employed in both works: while Navas *et al.* [22] used the Collocation method, in the present methodology, as previously explained, a central difference explicit Newmark's scheme is adopted. The former method is known to be able to damp high frequency solutions meanwhile the explicit method does not. However, although the explicit solution presents this oscillating behavior, the steady solution is reached successfully without any additional numerical damping. This clearly demonstrates the good performance of the present methodology even for zone III problems.

5.2 Large deformation consolidation

Some examples seen in literature propose the consolidation of a column of soil as a discretization of a semi-infinite domain. Our goal, however, is the validation of the presented methodology when large deformation occurs. Taking this into consideration, the consolidation problem solved by Li *et al.* [18] is taken as a reference since they proposed a methodology to explicitly solve the dynamic expulsion of fluid from the porous solid matrix. The geometry is seen in Fig. 1.A, a column of soil which is loaded in the way that is shown in Fig. 1.C. The loading increases to reach P_{max} at $t_0 = 0.05$ s, when the pressure is kept constant until the end of the simulation (0.5 s). The parameters employed for the soil skeleton are listed in Tab. 4. The Neo-Hookean material model proposed by Ehlers and Eipper [14], see Eq. (21), is assumed in this case.

The validation is made against the solution proposed by Li *et al.* [18]. The settlement of the top surface along time is checked for three different values of P_{max}, namely 2, 4 and 8 MPa. The obtained solutions are seen in Fig. 5 for all three cases. It can be seen that the final steady solution of the settlement fits very well the finite deformation reported by Li *et al.* for the three different loading conditions, as it was expected, since the finite deformation scheme is the one employed in the current research.
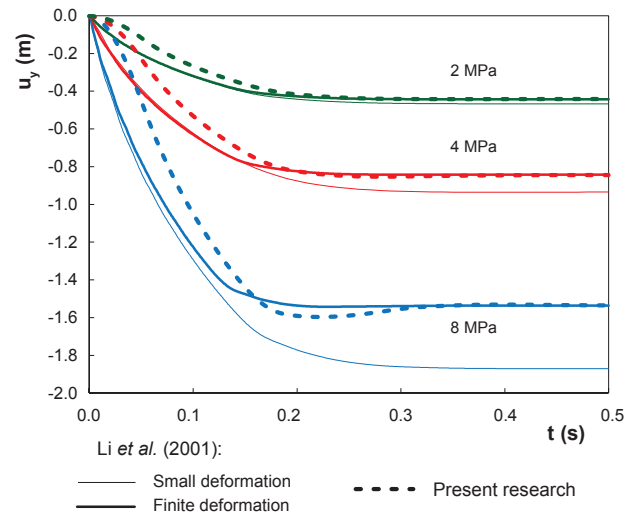
Fig. 5 Comparison between the settlement obtained by Li *et al.* [18] and with the current methodology for the large deformation consolidation problem.

With this example, we seek to verify that the correct settlement value is obtained upon reaching the steady state. Such a comparison is not possible along the entire process since Li *et al.* [18] assumed the $u - p_w$ formulation, which is suitable for slow phenomena, in a quasi static approach. By contrast, we have taken on the complete Biot's equations, which enables us to capture all the dynamic behaviors, since neither the soil nor the fluid accelerations are not neglected. Consequently, a ramped loading, contrary to the step-wise one employed in [18], is necessary in our case to avoid non-physical sudden loading.

Additionally, traditional Neo-Hookean law [6] and the modified one by Ehlers and Eipper [14] for soil compaction are tested and shown in Fig. 6. We can conclude that the modified law is much more convenient when compaction of the soil is modeled. With the Bonet's law we obtain bigger settlement than the expected one. This fact suggests that this law is not suitable to simulate the reduction of the pores volume, i.e. the compaction, which leads to the hardening of the soil and the lesser settlement.

5.3 Drainage of a square domain of saturated soil loaded by a rigid footing

In this Section, the current methodology is applied to the analysis of a representative square domain of saturated soil loaded on the top right half by a rigid footing. The same problem was previously studied by Sanavia *et al.* [27, 28]. The geometry and material properties are shown in Fig. 7. A displacement of 1 m on the loaded
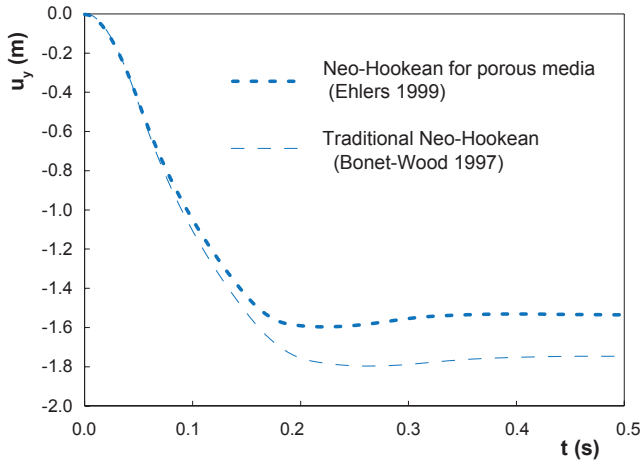
Fig. 6 Comparison between the settlement obtained with two different Neo-Hookean laws when a pressure of 8 MPa is applied.
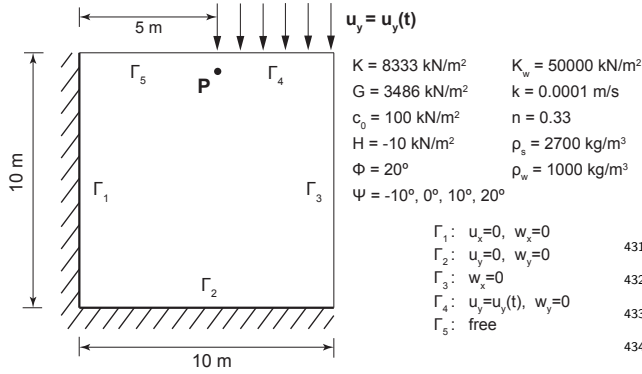

Fig. 7 Geometry, material parameters and boundary conditions of a square domain of water saturated porous material

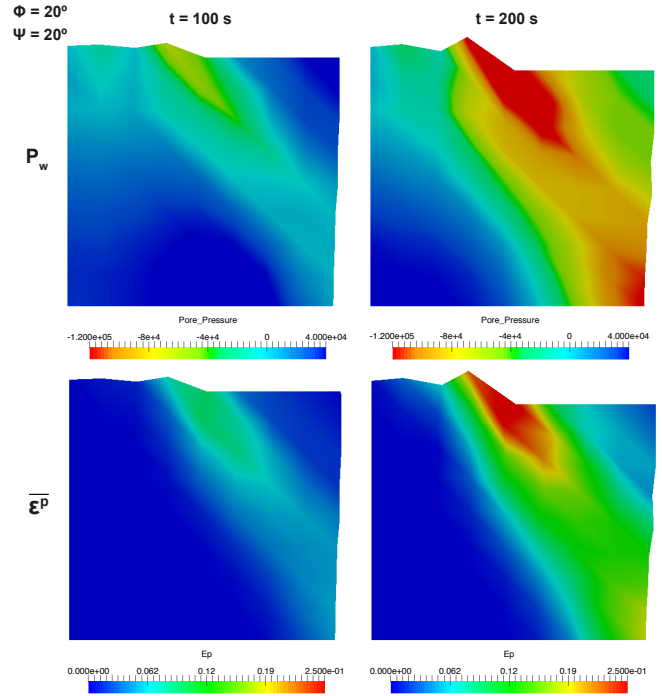**Fig. 8** Pore pressure (in Pa) and equivalent plastic strain at 100 s and 200 s of the square domain for $\psi = 20°$.

boundary, Γ_4, is imposed gradually during the simulation. Originally, a regular 8x8 discretization is employed, which corresponds to a nodal spacing of 1.25 m. The time step is of 5 ms. The importance of this example lies in fact that, depending on the dilatancy angle, the formation of the shear band and the deformation pattern as well as the pore pressure may vary. Firstly, the currently obtained solution is tested against the previously mentioned references, by applying the imposed displacement along 200 s ($5 \cdot 10^{-3}$ m/s) as a very slow loading condition. It is worth mentioning that this slow velocity in the application of the loading is required as the model we are comparing with is pseudo-static. The distribution of pore pressure and equivalent plastic strain can be seen in Fig. 8 at two different times of the simulation, being very similar to the previous solutions reported by Sanavia *et al.* [28].

Since this is a methodology assumed to be suitable to capture fast phenomena, further simulations are carried out with a faster loading velocity ($2 \cdot 10^{-2}$ m/s)

in order to check the good performance of the method against fully dynamic conditions. The obtained results on pore pressure and equivalent plastic deformation are shown in Figs. 9-17 for the different dilatancy angles of $20°$, $10°$, $0°$ and $-10°$ at 25 and 50 s respectively. For all the cases, the friction angle is kept at $20°$. It can be observed that there are no significant variation on the obtained equivalent plastic strain when the dilatancy angle changes. However, when the dilatancy angle decreases, a decrease of the shear band slope is noticed. In addition, the effect of the plastic dilatancy (contractancy) is evidenced by the negative (positive) pore pressure within the shear band zone, see Figs. 9-10 and Fig. 17 respectively. Moreover, in the case of zero dilatancy angle, see Fig. 11, no marked pore pressure variation is observed within the shear band zone. Similar phenomena were obtained by Sanavia *et al.* [28].

In order to study the evolution of the principal results of the problem, the histories of the pore pressure and equivalent plastic strain in a material point close to the shear band (Point P, see Fig. 7) have been depicted in Figs. 13 and 14.

For positive dilatancy values, smooth pore pressure evolution is observed. In addition, the peak pressure signals the initiation of plastic strain localization or shear band. The further extension of the shear band is accompanied by the continuous decreasing of the pore pressure. The material with dilatancy equal to $0°$ expe-
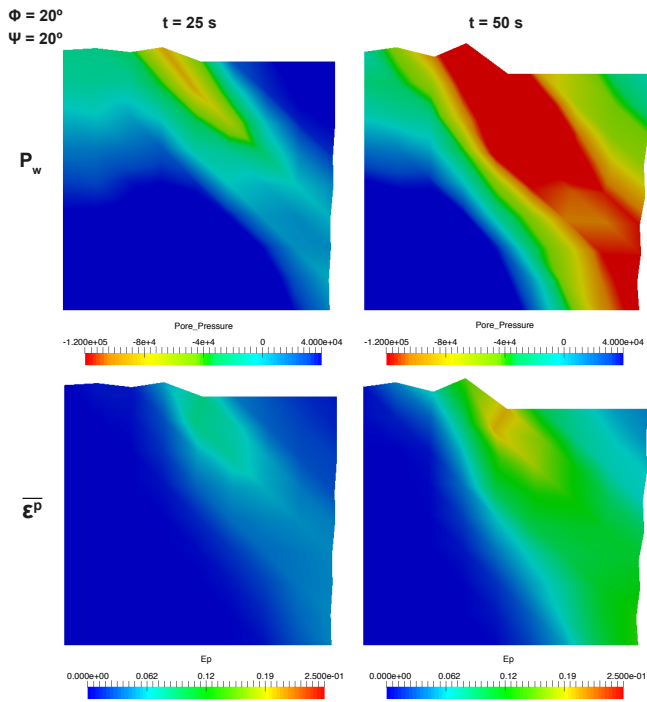
Fig. 9 Pore pressure (in Pa) and equivalent plastic strain at 25 s and 50 s the square domain for $\psi = 20°$.
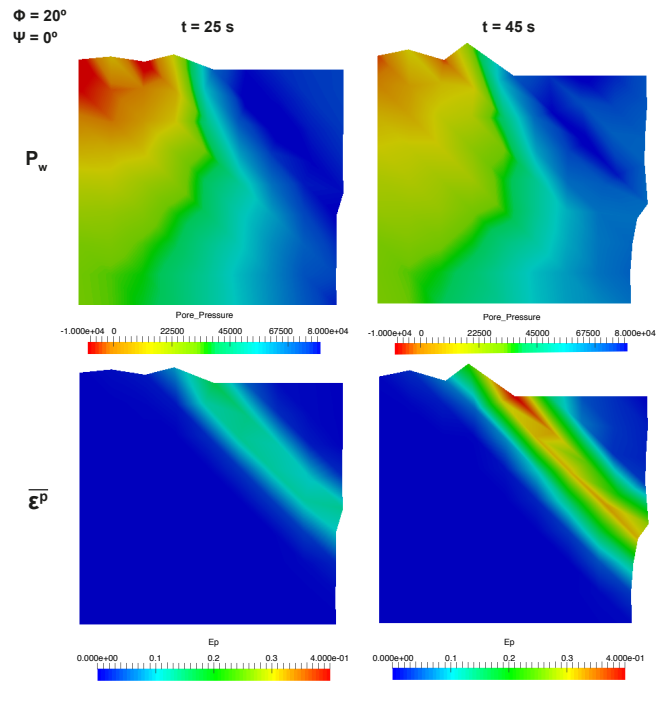

Fig. 11 Obtained results of the pore pressure (in Pa) and equivalent plastic strain at 25 s and 45 s of the square domain with $\psi = 0°$.
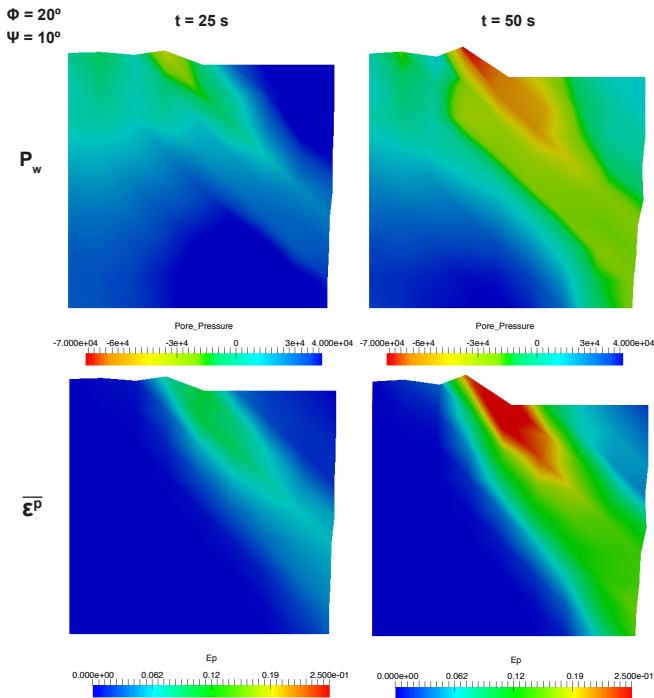

Fig. 10 Obtained results of the pore pressure (in Pa) and equivalent plastic strain at 25 s and 50 s of the square domain with $\psi = 10°$.
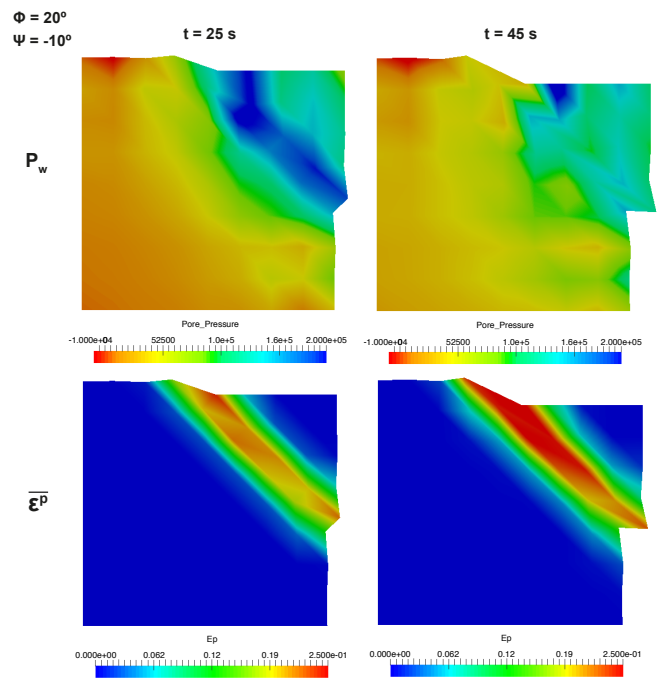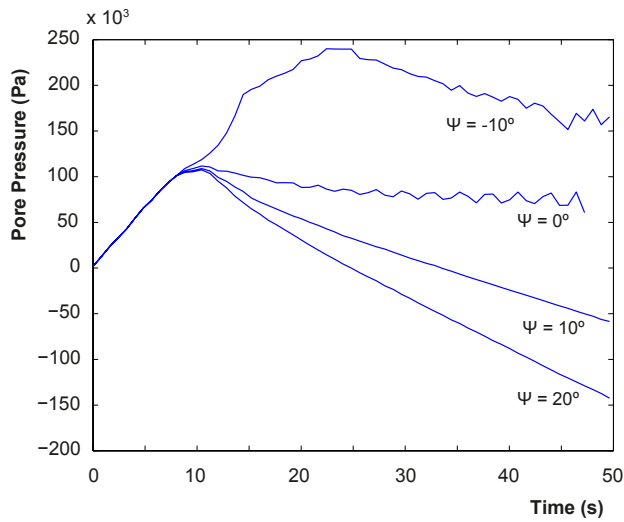

Fig. 12 Obtained results of the pore pressure (in Pa) and equivalent plastic strain at 25 s and 45 s of the square domain with $\psi = -10°$.

Fig. 13 Evolution of the pore pressure along the time in the point P.
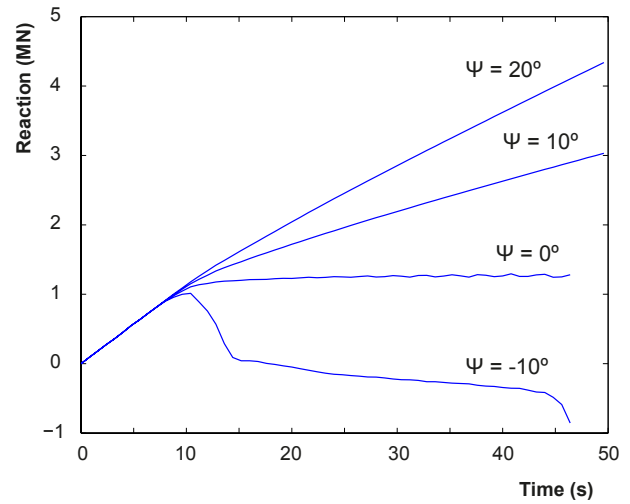
Fig. 15 Reaction forces of the soil for the different dilatancy angles.
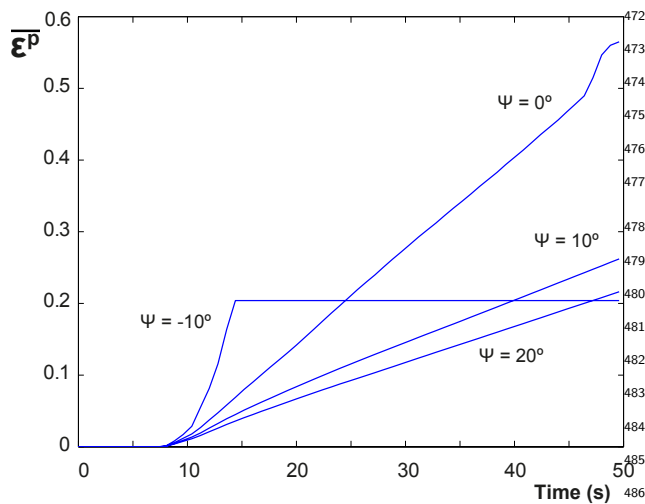
Fig. 14 Evolution of the equivalent plastic strain with time in the point P.

riences a softer decreasing, in this case due to the dissipation of the pore pressure in the permeable boundary, not because of the shear band. In addition, for zero and negative dilatancy angles, increased pore pressure oscillation is seen and finally leads to an instability in the last five seconds of the simulation. This is the reason why figures 11 and 17 are not depicted for 50 s, but for 45 s. The contractive behavior presents soil failure around 15 seconds. Before that point the pore pressure increases in the plastic zone; after that, the soil fails and there is no change of the plastic strain. This failure is also reflected in the reaction of the soil against this load, Fig. 15.

From Fig. 15, we observe that the reaction force for negative dilatancy angles presents a softening branch until the soil fails, i.e. when the reaction force approaches zero. By contrast, positive dilatancy angles presents a hardening branch whereas zero dilatancy angle shows a horizontal part with slightly increased oscillations.

The influence of the velocity of the loading can be seen by comparing Figs. 8 and 9. In the quicker problem the dissipation is slower and a higher pore pressure in the lower right corner is seen. In contrast, more negative values are seen in the shear band, what leads to a lower plastic strain values around that zone. This quicker reduction of the pore pressure with the higher loading rate is also observed in Fig. 18, where both solutions are compared along the displacement of the footing. The increase of the plastic strain due to the higher pore pressure is evident as well.

Finally, studies on the mesh dependency and the LME parameters are carried out. Three additional discretization levels, 12x12, 16x16 and irregular 10x14, are employed to refine the original one (8x8). Moreover, the original value of 1.4 for the shape parameter of the LME shape function, γ, see Eq. (47), has been tuned to 2.4 as well. The results of the pressure and the equivalent plastic strain at the final of the simulation are presented in Figs. 17, 18 and 19 for the cases of 12x12, 16x16 and 10x14, respectively.

It is observed that a finer discretization gives better resolution of the shear band, thus better pore pressure distribution. In addition, such enhancement is more pronounced with larger values of γ (which corresponds to smaller neighborhood). This is attributed to the fact
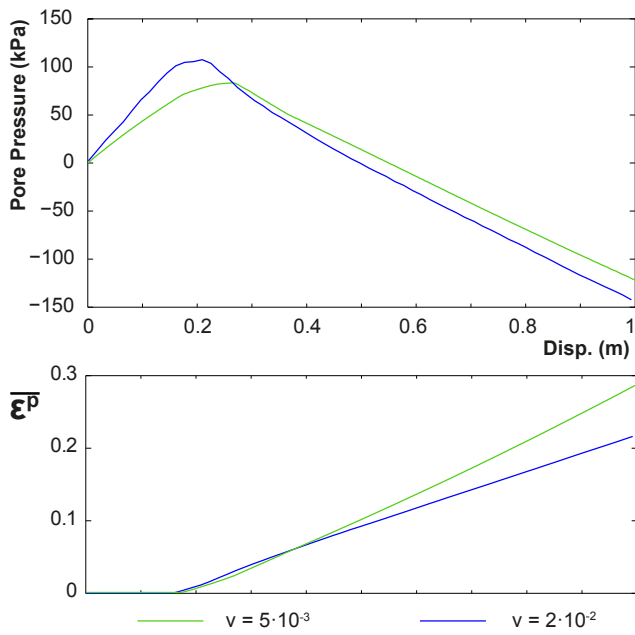
Fig. 16 Pore pressure and equivalent plastic strain obtained by each loading rate against the displacement of the footing.
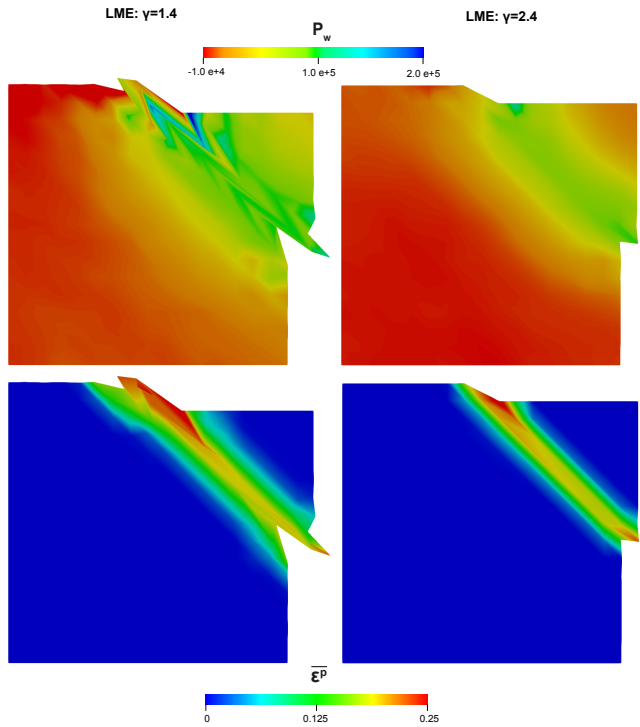

Fig. 18 Results of the pressure (upper row) and the equivalent plastic strain (lower row) for $\gamma=1.4$ (left column) and 2.4 (right column) at the final of the simulation for the discretization level of 16x16.
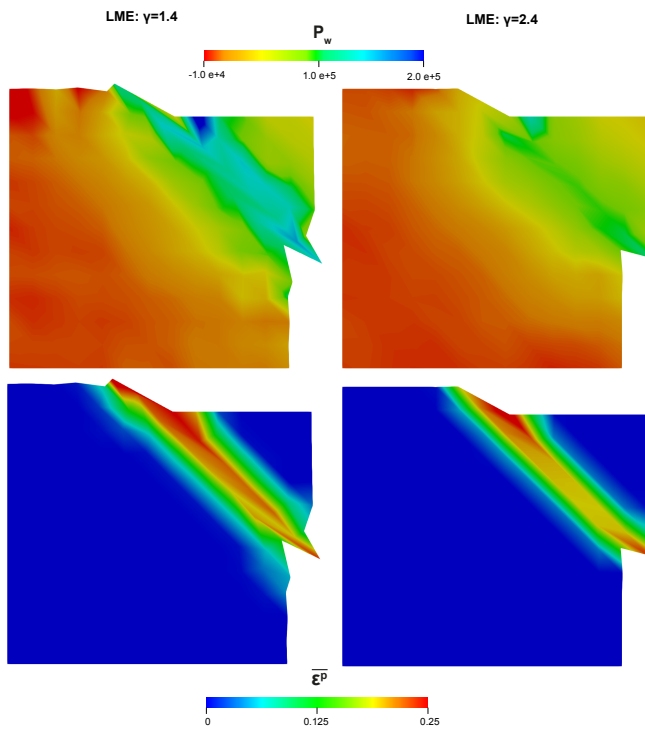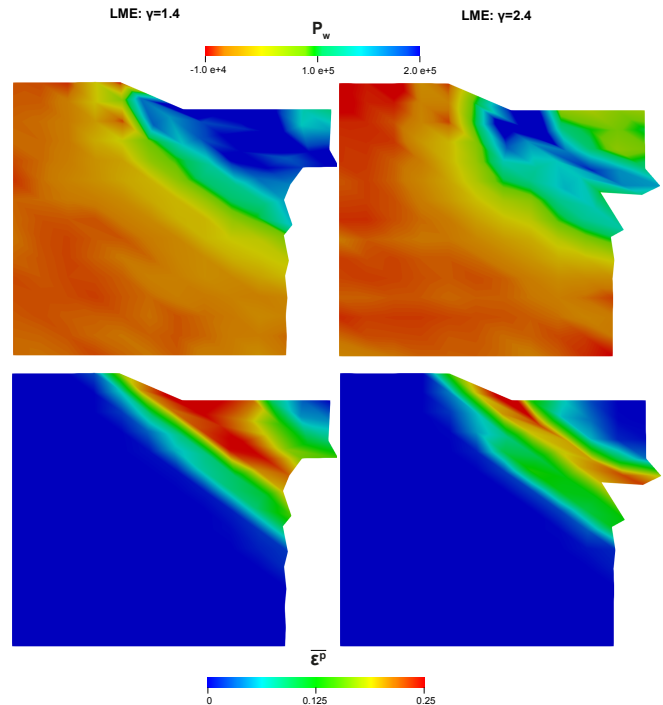

Fig. 17 Results of the pressure (upper row) and the equivalent plastic strain (lower row) for $\gamma=1.4$ (left column) and 2.4 (right column) at the final of the simulation for the discretization level of 12x12.

Fig. 19 Results of the pressure (upper row) and the equivalent plastic strain (lower row) for $\gamma=1.4$ (left column) and 2.4 (right column) at the final of the simulation for the discretization level of 10x14.

that, a smaller neighborhood reduces the spurious smoothing out of the shear band, see the results for $\gamma=1.4$.

In the case of irregular discretization, see Fig. 19, for pressure and plastic strain distribution, it is observed that in order to obtain the same level of accuracy, a finer level of discretization than regular ones is needed.

6 Conclusions

We have presented a new methodology to model biphase saturated soils, solving the coupled problem in an explicit manner. In order to extend this methodology to the dynamic range, the complete formulation of the Biot's equations is employed. Both elastic and plastic solid behaviors have been tested, meanwhile in the case of the water, the complete Darcy's law is simulated, taking into account the acceleration terms, which play an important role in some dynamic cases. Although this methodology has been carried out within the Local Max-Ent shape function, employing a spatial discretization based on the Optimal Transportation Meshfree scheme, the proposed model can be utilized for any other type of finite element method. Since the finite strain formulation is employed in order to be able to simulate large deformation regimes, advanced techniques such as any other meshfree scheme are well recommended.

Firstly, the model is employed under high frequency loading conditions and an elastic media. Zienkiewicz et al. [34] presented this problem and recently Navas et al. [22] solved it with an implicit methodology and dissipative time integration schemes. Compared to this former research, the proposed methodology yields very good trend, reproducing the original envelopes quite well. The main difference lies in the oscillation that the current results present, which was expected as the Central Differences explicit Newmark's scheme was used.

Secondly, the performance of the method under large deformation regime is analyzed. The first example carried out is a large consolidation that was proposed firstly by Li et al. [18]. Several simulations with different Neo-Hookean models are executed, giving the idea that the one proposed by Ehlers and Eipper [14] fits very well with the compaction behavior when large consolidation is modeled.

Finally, last example is performed within a Drucker-Prager flow rule in order to see the behavior of the pore pressure along the plastic shear bands depending on the dilatancy of the material. Sanavia et al. [28] verified that contractive materials accumulate pore pressure while in the dilatant shear band the reduction of pore pressure is observed. This behavior is well captured in the present research. Differences between both studies reside in the employment of inertial terms made by the complete Biot's formulation in the present research. Some pressure instabilities are found when large plastic strains occur, mainly when the soil experiences more contractive behavior.

A Nomenclature

- $\boldsymbol{a}^s \equiv \ddot{\boldsymbol{u}}$: acceleration vector of the solid = material time derivative of $\boldsymbol{v}^s$
- $\boldsymbol{a}^{ws}$: relative water acceleration vector with respect to the solid = material time derivative of $\boldsymbol{v}^{ws}$ with respect to the solid
- $\boldsymbol{b} = \boldsymbol{F}\boldsymbol{F}^T$: left Cauchy-Green tensor
- $\bar{\boldsymbol{b}}$: body forces vector
- c: cohesion (equivalent to the yield stress, σ_Y)
- $\boldsymbol{C} = \boldsymbol{F}^T\boldsymbol{F}$: right Cauchy-Green tensor
- $\boldsymbol{C}$ (time integration scheme): damping matrix
- $\frac{D^s\square}{Dt} \equiv \dot{\square}$: material time derivative of $\square$ with respect to the solid
- $\boldsymbol{F} = \frac{\partial \boldsymbol{x}}{\partial \boldsymbol{X}}$: deformation gradient
- $\boldsymbol{g}$: gravity acceleration vector
- G: shear modulus
- h: nodal spacing
- H: hardening modulus, derivative of the cohesion against time.
- $\boldsymbol{I}$: second order unit tensor
- $J = \det\boldsymbol{F}$: Jacobian determinant
- k: intrinsic permeability
- $\boldsymbol{k}$: permeability tensor
- K: bulk modulus
- K_s: bulk modulus of the solid grains
- K_w: bulk modulus of the fluid
- $\boldsymbol{M}$: mass matrix
- n: porosity
- $N(\boldsymbol{x})$, $\nabla N(\boldsymbol{x})$: shape function and its derivatives
- p: solid pressure
- p_w: pore pressure
- $\boldsymbol{P}$ (time integration scheme): external forces vector
- Q: volumetric compressibility of the mixture
- $\boldsymbol{R}$: internal forces vector
- $\boldsymbol{s} = \boldsymbol{\sigma}^{dev}$: deviatoric stress tensor
- t: time
- $\boldsymbol{u}$: displacement vector of the solid
- $\boldsymbol{U}$: displacement vector of the water
- $\boldsymbol{v}^s = \dot{\boldsymbol{u}}$: velocity vector of the solid
- $\boldsymbol{v}^{ws}$: relative velocity vector of the water with respect to the solid
- $\boldsymbol{w}$: relative displacement vector of the water with respect to the solid
- $Z(\boldsymbol{x}, \boldsymbol{\lambda})$: denominator of the exponential shape function

- α_F, α_Q and β: Drucker-Prager parameters
- β, γ: time integration schemes parameters
- β, γ: LME parameters related with the shape of the neighborhood
- $\Delta\gamma$: increment of equivalent plastic strain
- $\bar{\varepsilon}^p$: equivalent plastic strain
- $\boldsymbol{\varepsilon}$: small strain tensor
- ε_0: reference plastic strain
- κ: hydraulic conductivity
- λ: Lamé constant
- $\boldsymbol{\lambda}$: minimizer of $\log Z(\boldsymbol{x}, \boldsymbol{\lambda})$
- μ_w: viscosity of the water
- ν: Poisson's ratio
- ρ: current mixture density
- ρ_w: water density
- ρ_s: density of the solid particles
- $\boldsymbol{\sigma}$: Cauchy stress tensor
- $\boldsymbol{\sigma}'$: effective Cauchy stress tensor
- $\boldsymbol{\tau}$: Kirchhoff stress tensor
- $\boldsymbol{\tau}'$: effective Kirchhoff stress tensor
- Φ: plastic yield surface
- ϕ: friction angle
- ψ: dilatancy angle

Superscripts and subscripts

- ^{dev}: superscript for deviatoric part
- ^{e}: superscript for elastic part
- $_k$: subscript for the previous step
- $_{k+1}$: subscript for the current step
- ^{p}: superscript for plastic part
- ^{s}: superscript for the solid part
- ^{trial}: superscript for trial state in the plastic calculation
- ^{vol}: superscript for volumetric part
- ^{w}: superscript for the fluid part
- ^{ws}: superscript for the fluid part relative to the solid one

References

1. Armero, F.: Formulation and finite element implementation of a multiplicative model of coupled poro-plasticity at finite strains under fully saturated conditions. Computer Methods in Applied Mechanics and Engineering **171**, 205–241 (1999)

2. Arroyo, M., Ortiz, M.: Local maximum-entropy approximation schemes: a seamless bridge between finite elements and meshfree methods. International Journal for Numerical Methods in Engineering **65**(13), 2167–2202 (2006)

3. Bandara, S., Soga, K.: Coupling of soil deformation and pore fluid flow using material point method. Computers and Geotechnics **63**, 199–214 (2015)

4. Biot, M.A.: General solutions of the equations of elasticity and consolidation for a porous material. Journal of Applied Mechanics pp. 91–96 (1956)

5. Biot, M.A.: Theory of propagation of elastic waves in a fluid-saturated porous solid. I. Low-Frequency range. Journal of the Acoustical Society of America **28**(2), 168–178 (1956)

6. Bonet, J., Wood, R.: Nonlinear continuum mechanics fot finite element analysis. Cambridge University Press,The Pitt Building, Trumpington Street, Cambridge, UK (1997)

7. Borja, R., Alarcón, E.: A mathematical framework for finite strain elastoplastic consolidation. part1: balance laws, variational formulation, and linearization. Computer Methods in Applied Mechanics and Engineering **122**, 145–171 (1995)

8. Borja, R., Alarcón, E.: Elastoplastic consolidation at finite strain. part 2: finite element implementation and numerical examples. Computer Methods in Applied Mechanics and Engineering **159**, 103–122 (1998)

9. Camacho, G., Ortiz, M.: Adaptive lagrangian modelling of ballistic penetration of metallic targets. Computers methods in applied mechanics and engineering **142**, 269–301 (1997)

10. Cao, T., Sanavia, L., Schrefler, B.: A thermo-hydro-mechanical model for multiphase geomaterials in dynamics with application to strain localization simulation. international Journal for Numerical methods in Engineering **107**, 312–337 (2016)

11. Ceccato, F., Simonini, P.: Numerical study of partially drained penetration and pore pressure dissipation in piezocone test. Acta Geotechnica **12**, 195–209 (2016)

12. Cuitiño, A., Ortiz, M.: A material-independent method for extending stress update algotithms from small-strain plasticity to finite plasticity with multiplicative kinematics. Engineering computations **9**, 437–451 (1992)

13. Diebels, S., Ehlers, W.: Dynamic analysis of fully saturated porous medium accounting for geometrical and material non-linearities. International Journal for Numerical Methods in Engineering **39**, 81–97 (1996)

14. Ehlers, W., Eipper, G.: Finite elastic deformations in liquid-saturated and empty porous solids. Transport in Porous Media **34**, 179–191 (1999)

15. Jeremić, B., Cheng, Z., Taiebat, M., Dafalias, Y.: Numerical simulation of fully saturated porous materials. International Journal for Numerical and Analytical Methods in Geomechanics **32**, 1635–1660 (2008)

16. Lewis, R., Schrefler, B.: The finite element method in the static and dynamic deformation and consolidation of porous media. John Wiley & Sons Ltd. (1998)

17. Li, B., Habbal, F., Ortiz, M.: Optimal transportation meshfree approximation schemes for fluid and plastic flows. International Journal for Numerical Methods in Engineering **83**, 1541–1579 (2010)

18. Li, C., Borja, R.I., Regueiro, R.A.: Dynamics or porous media at finite strain. Computed Methods in Applied Mechanics and Engineering **193**, 3837–3870 (2004)

19. López-Querol, S., Blazquez, R.: Liquefaction and cyclic mobility model in saturated granular media. International Journal for Numerical and Analytical Methods in Geomechanics **30**, 413–439 (2006)

20. López-Querol, S., Fernández-Merodo, J., Mira, P., Pastor, M.: Numerical modelling of dynamic consolidation on granular soils. International Journal for Numerical and Analytical Methods in Geomechanics **32**, 1431–1457 (2008)

21. Navas, P., López-Querol, S., Yu, R., Li, B.: B-bar based algorithm applied to meshfree numerical schemes to solve unconfined seepage problems through porous media. International Journal for Numerical and Analytical Methods in Geomechanics **40**, 962–984 (2016)

22. Navas, P., López-Querol, S., Yu, R., Li, B.: Meshfree methods applied to consolidation problems in saturated soils, pp. 241–264. Innovative numerical approaches for coupled multi-scale problems. Springer (2016)

23. Navas, P., López-Querol, S., Yu, R., Pastor, M.: Large deformation analysis of failure of shallow foundations using

the optimal transportation meshfree method. Geotechnique **Under review**, – (2017)

24. Ortiz, A., Puso, M., Sukumar, N.: Construction of polygonal interpolants: A maximum entropy approach. International Journal for Numerical Methods in Engineering **61**(12), 2159–2181 (2004)

25. Ravichandran1, N., Muraleetharan, K.: Dynamics of unsaturated soils using various finite element formulations. International Journal for Numerical and Analytical Methods in Geomechanics **33**, 611–631 (2009)

26. Sanavia, L., Pesavento, F., Schrefler, B.: Finite element analysis of non-isothermal multiphase geomaterials with application to strain localization simulation. Computational Mechanics **37(4)**, 331–348 (2006)

27. Sanavia, L., Schrefler, B., Stein, E., Steinmann, P.: Modelling of localisation at finite inelastic strain in fluid saturated porous media. Proc. In: Ehlers W (ed.), IUTAM Symposium on Theoretical and Numerical Methods in Continuum Me- chanics of Porous Materials, Kluwer Academic Publishers pp. 239–244 (2001)

28. Sanavia, L., Schrefler, B., Steinmann, P.: A mathematical and numerical model for finite elastoplastic deformations in fluid saturated porous media. In: G. Capriz, V. Ghionna, P. Giovine (ed.) Modeling and Mechanics of Granular and Porous Materials, Series of Modeling and Simulation in Science, Engineering and Technology pp. 297–346 (2001)

29. Sanavia, L., Schrefler, B., Steinmann, P.: A formulation for an unsaturated porous medium undergoing large inelastic strains. Computational Mechanics **28**, 137–151 (2002)

30. Terzaghi, K.V.: Principles of Soil Mechanics. Engineering News-Record **95**, 19–27 (1925)

31. Ye, F., Goh, S., Lee, F.: A method to solve biot's u-u formulation for soil dynamic applications using the abaqus/explicit platform. Numerical Methods in Geotechnical Engineering pp. 417–422 (2010)

32. Zienkiewicz, O., Chan, A., Pastor, M., Paul, D., Shiomi, T.: Static and dynamic behaviour of geomaterials: A rational approach to quantitative solutions. part i: Fully saturated problems. Proc. Roy. Soc. Lond. **A429**, 285–309 (1990)

33. Zienkiewicz, O., Chan, A., Pastor, M., Schrefler, B., Shiomi, T.: Computational Geomechanics. John Wiley, UK (1999)

34. Zienkiewicz, O., Chang, C., Bettes, P.: Drained, undrained, consolidating and dynamic behaviour assumptions in soils. Géotechnique **30**(4), 385–395 (1980)

35. Zienkiewicz, O., Shiomi, T.: Dynamic behaviour of saturated porous media: The generalized biot formulation and its numerical solution. Int. J. Num. Anal. Geomech. **8**, 71–96 (1984)